A finite-element based numerical tool for $Ni_{47}Ti_{44}Nb_9$ SMA structures design: application to tightening rings

B. Piotrowski[a,b,c], T. Ben Zineb[a], E. Patoor[b], A. Eberhardt[b]

[a]*Laboratoire d'Energétique et de Mécanique Théorique et Appliquée (LEMTA), Nancy University, CNRS, 2 rue Jean Lamour; 54500 Vandoeuvre-les-Nancy, France*
[b]*Laboratoire d'Etude des Microstructures et de Mécanique des Matériaux (LEM3), Paul Verlaine University, Arts et Métiers ParisTech, ENIM, CNRS, Ile du Saulcy; 57045 Metz cedex 01, France*
[c]*Etudes et Productions Schlumberger, 1 rue Henri Becquerel, 92140, Clamart France*

Abstract

This paper deals with the design of $Ni_{47}Ti_{44}Nb_9$ Shape Memory Alloy (SMA) tightening components. The tightening of an SMA ring on an elastic pipe is analyzed using the finite element code ABAQUS® and a UMAT subroutine developed in our group to model the specific behavior of $Ni_{47}Ti_{44}Nb_9$ SMA. Main features of the thermomechanical model implemented in this UMAT routine are briefly recalled.

Numerical predictions are validated using experimental tightening pressures obtained on a test bed developed in this work. The validation strategy is documented and the results for different ring thicknesses are presented. This finite element tool is then applied to a parametric study of the influence of ridges on the tightening pressure. Eventually, geometrical defects like out of roundness are considered.

Key words: Shape Memory Alloy, Numerical simulation, Model validation, Recovery stress

1. Introduction

Sealing solutions are often required in various industrial areas. One of the requirement is to ensure a connection between two pipes. Among the various solutions proposed, those using SMA rings stand out (Kauffman and Mayo, 1996). Their simplicity involving only heating at a moderate temperature and their reliability are major advantages. NiTi rings are often adopted, but they are restricted by the narrow temperature range in which this application can operate. The low transformation temperature hysteresis of NiTi SMA is responsible for the narrow size of the operating domain ; typically about 50 °C. The occurence of plastic strain into NiTi SMA induces a hysteresis enlarging and improves the application field. However, the amount of plastic strain required to enlarge significantly the transformation temperature hysteres has a negative impact on the shape memory properties. Fe-based SMA are known for their abilities to exhibit plastic strain without important loss of shape memory capability, but their lack of corrosion resistance makes them unusable in major industrial applications. $Ni_{47}Ti_{44}Nb_9$ SMA was developed to

overcome these limitations (Melton et al., 1989). Specific composition combined with adapted thermo-mechanical treatments strongly increase the hysteresis size. The presence of elastic-plastic niobium inclusions explains this particular behavior (Zhang et al., 1991). $Ni_{47}Ti_{44}Nb_9$ SMA is consequently often considered in industrial applications as connectors, sealing rings and clamping components. Despite its importance for industry, $Ni_{47}Ti_{44}Nb_9$ SMA has been attracted very little attention in research works. A thermo-mechanical model was only recently proposed (Piotrowski, 2010; Piotrowski et al., 2011). It considers niobium precipitates as elastic-plastic inclusions embedded in a NiTi matrix. This model has been implemented in the finite element code ABAQUS®. To be able to use it as a numerical tool for industrial applications design, a validation protocol is proposed. The aim is to evaluate the model's ability to accurately predict the $Ni_{47}Ti_{44}Nb_9$ behavior from the comparison between numerical simulations and experimental values obtained for some specific cases.

Various specimen shapes and different loading cases have been proposed to validate shape memory alloy models. A wire shape sample is often used (Chemisky et al., 2011; Saint-Sulpice et al., 2009; Zaki and Moumni, 2007; De la Flor et al., 2006). Other research homogeneous tensile test on dog bone shaped plate samples (Peultier et al., 2006), tension-torsion on thin-wall samples (Panico and Brinson, 2007), compression tests on bar and springs (Hartl et al., 2010) and bulging tests (Vieille et al., 2007). Tightening devices have also been used. Videnic et al. (2007) have studied the constrained recovery in a thick-walled SMA ring. Peultier et al. (2008) have developed a device which consists of the tightening of a shape memory ring on an elastic one.

As $Ni_{47}Ti_{44}Nb_9$ alloy is mostly considered for tightening applications, a validation protocol with tightening rings has been adopted for this study. This protocol is detailed in the next section. Tightening pressure evolution with temperature is recorded for two SMA ring thicknesses. Main features of the thermomechanical model used in this work are also given in section two. In the third section of this paper, experimental data obtained and numerical predictions are compared and discussed to validate the $Ni_{47}Ti_{44}Nb_9$ model. Model limitations are highlighted. This validation allows to study the structural effect influence in more complex devices in order to improve their tightening efficiency. A parametric study highlighting the geometric characteristics influence of ring having ridges is presented to illustrate the capabilities of the numerical model for component design optimization. Eventually, this numerical tool is applied to explain the sealing defect that occurred in some application cases.

2. Validation protocol

In this section, the studied device is presented. Experimental and numerical investigations of the device are performed, following the same tightening cycle. After a presentation of this cycle, numerical and experimental parts are described.

2.1. Studied device

The developed experimental device to monitor the tightening pressure provided by an SMA ring is presented in Fig. 1. It is composed of a $Ni_{47}Ti_{44}Nb_9$ ring and an Inconel 718 one with a high yield stress allowing a large range of tightening level with an elastic behavior. The internal diameter of the first one is DR_I, thickness is t_R and length L_R. The Inconel 718 external diameter is DP_E, thickness is t_P and length L_P. The thermoelastic material parameters of Inconel 718 are a Young modulus of 205 GPa, a Poisson ratio coefficient of 0.29 and a thermal expansion coefficient of 13 $\mu m/(m°C)$. The plastic yield stress is about 1000 MPa.
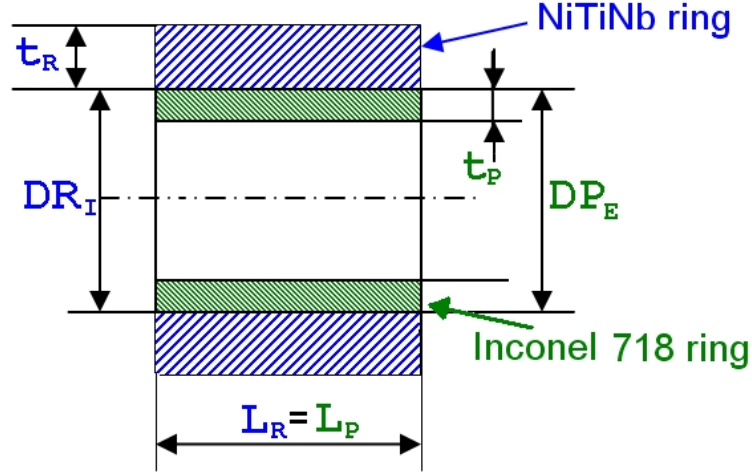
Figure 1: Device analyzed by experimental and numerical way - Ni$_{47}$Ti$_{44}$Nb$_9$ ring tightening on Inconel elastic ring Piotrowski (2010)

Two Ni$_{47}$Ti$_{44}$Nb$_9$ rings are supplied by Intrinsic Devices in an "opened state" and internal diameters before opening are unknown. The two configurations, called "thin" and "thick", are summarized in Tab. 1. Rings are chosen so that internal diameter after opening is equal in both configurations, but with various thicknesses. "Thin" and "thick" rings are supplied with different length. The ratio t_R/L_R is of 0.058 in thin configuration, and 0.352 in thick. Elastic ring is chosen in order to have the same length as the Ni$_{47}$Ti$_{44}$Nb$_9$ one, to avoid edge effects.

Table 1: Ring dimension in the two configurations

N°	Reference	DR_I (mm)		t_R	L_R
	NiTiNb ring	opened	heated	(mm)	(mm)
1-thin Tn	AHM2565-0089-1526	25.65	24.59	0.89	15.26
2-thick Tck	AHM2565-0358-1016	25.65	24.47	3.58	10.16
N°	t_R/L_R	DP_E	t_P	L_P	
		(mm)	(mm)	(mm)	
1-thin	0.058	25.50	1.75	15.55	
2-thick	0.352	25.50	1.75	10.40	

2.2. Tightening cycle

The tightening cycle is presented in Figure 2, where conditioning and implementation cycle are represented. Four characteristic temperatures have to be considered for tightening applications in the described cycle:

- T_1 is the temperature at which the SMA ring is opened (conditioning). Pressure is applied on the ring internal face. The SMA has to be in the martensitic state. That means that

3

T_1 must be lower than the M_f temperatures, $(T_1 < M_f)$. The pressure induces martensitic reorientation. Once the pressure is released (step 3), an elastic return occurs and the clearance between the two rings is equal to $g/2$.

- The SMA ring is placed around an elastic one, and the device is heated. T_2 is the temperature at which the reverse transformation mechanism begins during heating. It is the $Ni_{47}Ti_{44}Nb_9$ characteristic transformation temperature A_s. Then, increasing temperature induces a decrease of the SMA ring's internal diameter by reverse transformation. After contact between the two rings, tightening pressure appears.

- T_3 is the temperature to which the device must be heated to obtain maximum tightening by complete reverse transformation. This temperature is related to A_f temperature and to the stress state.

- T_4 is the temperature below which the martensitic transformation occurs and consequently the device loses its tightness.
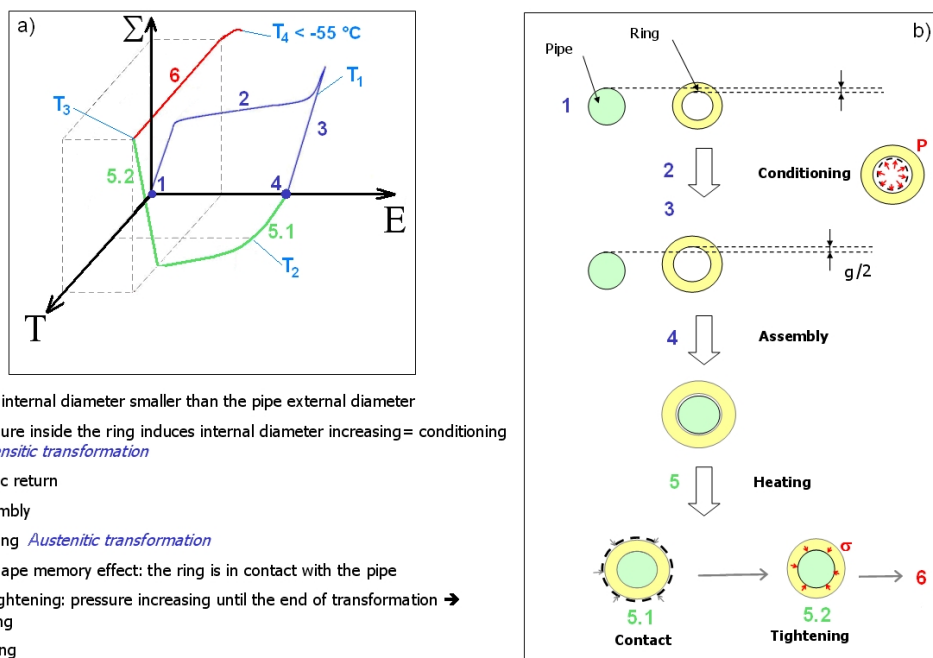

1 : Ring internal diameter smaller than the pipe external diameter

2 : Pressure inside the ring induces internal diameter increasing = conditioning
Martensitic transformation

3 : Elastic return

4 : Assembly

5 : Heating *Austenitic transformation*

5.1 : Shape memory effect: the ring is in contact with the pipe

5.2 : Tightening: pressure increasing until the end of transformation ➔ sealing

6 : Cooling

Figure 2: Applied thermo-mechanical cycle on a shape memory ring - a) Stress (Σ) -strain (E) - temperature (T) diagram - b) Corresponding tightening steps (g is the clearence between internal diameter of the SMA ring and the external one of the tube after elastic return)

By comparison with $Ni_{47}Ti_{44}Nb_9$, the main disadvantage of classical NiTi, for tigthening applications, is that the range of temperature between forward (M_s) and reverse (A_f) transformation temperatures is quite narrow (Miyazaki et al., 1982). Indeed, some applications need T_2 to be higher than room temperature to avoid reverse transformation during device transport, and T_4 to

be lower than -55 °C to avoid device disassembly during air transport and storage at low temperatures.

The studied device follows this tightening cycle. In the following sections, numerical and experimental investigations are described.

2.3. Numerical investigations

$Ni_{47}Ti_{44}Nb_9$ model

In this numerical section, the model describing the $Ni_{47}Ti_{44}Nb_9$ thermomechanical behavior is briefly presented, followed by the finite element model of the studied device. A model has
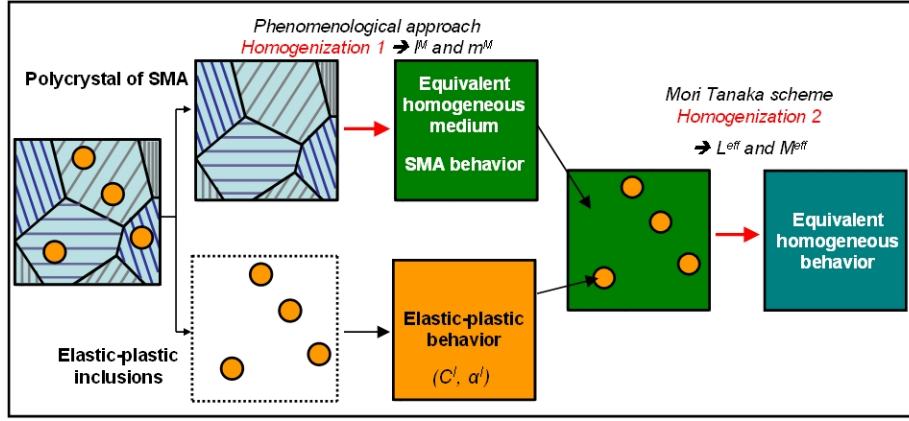

Figure 3: Homogenization strategy leading from SMA polycrystalline matrix with spherical elastoplastic inclusions to equivalent homogeneous medium (Piotrowski, 2010)

been proposed leading to effective constitutive equations of the studied alloy (Piotrowski et al., 2011; Chemisky et al., 2009). Experimental investigations of $Ni_{47}Ti_{44}Nb_9$ show Nb-rich precipitates embedded into a matrix phase mainly composed of NiTi. They have also shown that Nb-rich precipitates exhibit an elastic-plastic behavior. They are considered as homogeneously distributed inclusions into a NiTi matrix, with a low volume fraction (10 %) (Zhang et al., 1991). Considering this microstructure, the Mori-Tanaka transition scale scheme is adopted to derive the effective thermo-mechanical constitutive law, as illustrated in Fig. 3 (M and I respectively denote *Matrix* and *Inclusion*). The RVE is composed of SMA Matrix (NiTi) with niobium inclusions. Inclusions are assumed to have a spherical shape and their behavior is described by an elastic-plastic model (Wilkins, 1964; Simo and Hughes, 2000) which leads to the following elastic-plastic constitutive equation:

$$\dot{\sigma}_{ij}^I(r) = l_{ijkl}^I(r)\dot{\varepsilon}_{kl}^I(r) - c_{ijkl}^I(r)\alpha_{kl}^I\dot{T} \tag{1}$$

l^I is the mechanical tangent operator, and c^I and α^I are respectively the fourth order elastic tensor and the second order thermal expansion tensor.

NiTi matrix behavior is described with a macroscopic model (Chemisky et al., 2011). This model takes into account the main SMA physical phenomena and its material parameters are easy to identify. The SMA matrix constitutive law is derived incrementally (Eqn. 2):

$$\dot{\sigma}_{ij}^M(r) = l_{ijkl}^M(r)\dot{\varepsilon}_{kl}^M(r) - m_{ij}^M\dot{T} \tag{2}$$

l^M and m^M are respectively the mechanical and thermal tangent operators. More details about this model and the management of specific behaviors as saturation, internal loop and tension-compression asymmetry are developed in Chemisky et al. (2011).

Constitutive models of each phase are introduced in the Mori-Tanaka scale transition scheme in order to obtain the effective behavior. This results in an implicit problem which was numerically solved by an iterative approach based on the return mapping and the Newton-Raphson scheme. The strain inside each phase is defined as follow (Eqn. 3 and 4):

$$\dot{\varepsilon}^I_{mn} = A^{MT}_{mnij} \dot{E}_{ij} \tag{3}$$

$$\dot{\varepsilon}^M_{mn} = \frac{1}{1-z}((I_{mnij} - zA^{MT}_{mnij})\dot{E}_{ij}) \tag{4}$$

with the Mori-Tanaka transition scale tensor (Eqn. 5):

$$A^{MT}_{mnij} = [I_{ijmn} - (1-z)T^{II}_{ijkl}(l^M_{klmn} - l^I_{klmn})]^{-1} \tag{5}$$

Strain in inclusion and in matrix can derived from macroscopic strain (3, 4). Consequently, by taking into account the constitutive equations for matrix (2) and inclusion (1), the effective constitutive law is derived as follow:

$$\dot{\Sigma}_{ij} = z\dot{\sigma}^I_{ij} + (1-z)\dot{\sigma}^M_{ij} = L^{eff}_{ijmn}\dot{E}_{mn} - M^{eff}_{ij}\dot{T} \tag{6}$$

with the mechanical and thermal effective tangent operators (Eqn. 7,8):

$$L^{eff}_{ijmn} = z(l^I_{ijkl} - l^M_{ijkl})A^{MT}_{klmn} + l^M_{ijmn} \tag{7}$$

$$M^{eff}_{ij} = m^M_{ij} + z(c^I_{ijkl}\alpha^I_{kl} - m^M_{ij}) \tag{8}$$

Material parameters have been identified thanks to experimental tests (Piotrowski, 2010; He et al., 2006; Xiao et al., 2008; Liu et al., 2006; Wang et al., 2008). Table 2 summarizes identified parameter values for $Ni_{47}Ti_{44}Nb_9$ simulations. E^M, ν^M, α^M and E^I, ν^I, α^I represent respectively thermoelastic behavior in matrix and inclusion (Young modulus, Poisson ratio, thermal expansion) which is assumed to be isotropic. The matrix phase transformation parameters are the maximal transformation strain in tension (ε^T_{trac}) and compression (ε^T_{comp}), the transformation temperatures (M_s and A_f), their variation with stress (b), an internal loop parameter (r_f), the critical reorientation stress ($F^{max}_{\dot{\varepsilon}^T}$) and three interaction parameters (H_f, H_ε and H_{twin}). The plastic inclusion parameters are the elastic Yield stress (σ^Y) and two hardening parameters (H^{iso} and n). z parameter represents the inclusion volume fraction.

A resolution algorithm of the implicit system has been proposed. In the first iteration, strain inside matrix and inclusion are assumed to be equal to effective strain. Matrix and inclusion constitutive equations are unbalanced by this strain. Stress, tangent operators and internal variables of each phase are then computed. Mori-Tanaka tensor is also calculated, which gives the consistent values of strain into each phase. These strains are then compared to the initial ones, and corrected by a Newton Raphson algorithm.

Table 2: $Ni_{47}Ti_{44}Nb_9$ material parameters adopted for simulations

Parameter	Unit	Description	Value	Origin
E^M	MPa	SMA Young modulus	80000	Nanoindentation
ν^M	-	SMA Poisson ratio	0.3	$Ni_{51}Ti_{49}$
α^M	μm/(m °C)	Thermal expansion coefficient	8	(He et al., 2006)
ε^T_{trac}	-	Maximal transformation strain in tension	0.02	$Ni_{51}Ti_{49}$
ε^T_{comp}	-	Maximal transformation strain in compression	0.016	$Ni_{51}Ti_{49}$
b	MPa/ °C	Transformation temperatures variation with stress	10	(Liu et al., 2006)
M_s	°C	Martensite start temperature	-101	DSC
A_f	°C	Austenite finish temperature	63	DSC
r_f	-	Internal loop parameter	0.7	$Ni_{51}Ti_{49}$
$F^{max}_{\bar{\varepsilon}^T}$	MPa	Critical reorientation stress	125	(Xiao et al., 2008)
H_f	MPa	Transformation interaction parameter	5	$Ni_{51}Ti_{49}$
H_ε	MPa	Orientation interaction parameter	2100	$Ni_{51}Ti_{49}$
H_{twin}	MPa	Twin accommodation parameter	40000	$Ni_{51}Ti_{49}$
E^I	MPa	Inclusion Young modulus	53000	(Nemat-Nasser and Guo, 2000)
ν^I	-	Inclusion Poisson ratio	0.3	(Nemat-Nasser and Guo, 2000)
α^I	μm/(m °C)	Thermal expansion coefficient	8	(He et al., 2006)
σ^Y	MPa	Inclusion plastic yield stress	70	(Nemat-Nasser and Guo, 2000)
H^{iso}	MPa	Plastic hardening parameter	450	(Nemat-Nasser and Guo, 2000)
n	-	Plastic hardening parameter	4	(Nemat-Nasser and Guo, 2000)
z	-	Inclusion volume fraction	0.1	SEM

Finite Element Model

The studied device is composed of an axisymmetric geometry, loading and boundary conditions. Thus, an axisymmetric model is considered. Quadrilateral axisymmetric elements (CAX4R) are adopted to mesh the rings. A reduced integration technique is considered. Additional simulations were carried out by using complete integration elements (CAX4). Obtained results were close to those with reduced integration elements. For the thin ring, an element size of 0.22 mm is chosen in order to have 4 elements in the thickness. In the thick one, an element size of 0.60 mm is chosen, which induces 6 elements in thickness. It has been verified that such element sizes lead to the convergent results. Figure 4 represents the axisymmetric mesh for the two configurations. For more clarity a 3D representation, obtained by a revolution, is proposed.

Inconel elastic behavior is taken into account with an isotropic elastic model. A plastic yield stress at 1000 MPa is considered. $Ni_{47}Ti_{44}Nb_9$ implemented model is called by ABAQUS® via the UMAT subroutine. The applied cycle is composed of 5 steps: from an initial austenitic ring, a cooling until -175 °C is applied to form twinned martensite. Then, the internal diameter of the SMA ring is increased by applying uniform pressure. The elastic ring is placed into the SMA one, and heating to 175 °C induces the reverse transformation and the tightening. Finally, cooling is applied to -30 °C. A finite sliding frictionless contact, with "hard contact" normal behavior, is considered.

A preliminary study was conducted to determine the initial $Ni_{47}Ti_{44}Nb_9$ rings internal diameters: they are opened by the supplier Intrinsic Devices before delivery. The internal diameter before this step is unknown. The opening of the ring is through the orientation of twinned martensite variants, and it generates gradients of properties in the ring. It is essential to model this stage of the tightening cycle to accurately describe the real case. For both rings, simulations are performed with opening several internal diameter values, until the value after opening is identical to that of the ring provided.
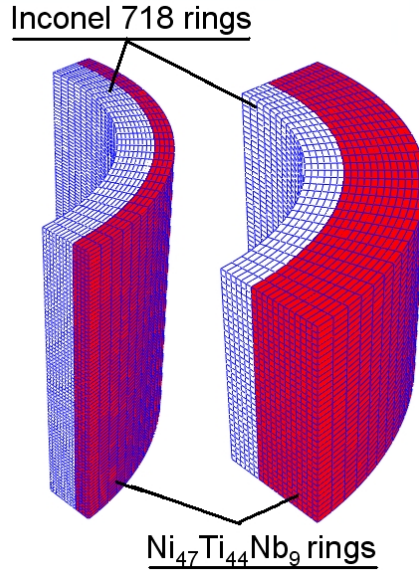
Figure 4: Axisymmetric meshes of studied device composed of Inconel 718 rings (white) and $Ni_{47}Ti_{44}Nb_9$ rings (red) - Mesh of thin (left) and thick (right) configurations (The axisymmetric mesh is represented in a 3D way by revolution)

Thick ring case. The ring diameter when opened is 25.94 mm. The transformation strain is assumed to reach its saturation value (2 %) at the opening of the ring. Several simulations have been conducted, and the determined initial internal diameter of the ring is 25.30 mm.

Thin ring case. The ring diameter in its opened state is 25.90 mm, and the determined initial internal diameter of the ring is 25.34 mm.

Numerical results

The tightening pressure evolution with temperature is presented in the validation section. Fig. 5 shows the tightening pressure of each ring at 175 °C (end of reverse transformation) and at 15 °C (room temperature, after tightening). It can been seen that the tightening pressure slightly decreases during cooling. This phenomenon is due to the thermal expansion and martensitic transformation is not active. Moreover, it can be seen that the thickness ratio between thin and thick rings (0.249) is close to the tightening pressure ratio at 175 °C (0.253).

The SMA ring stress field evolution during loading cycle is represented in Fig. 6. During the opening process, the internal pressure is more important in the thick case. Nevertheless, the stress field to achieve complete reorientation of martensite variants is higher in the thin ring. A stress gradient can be observed in the thick configuration. At the end of reverse transformation, around 175 °C, the stress field into the thick ring in the neighbourhood of the contact area is close to the stress field in the thin one. At the end of the cooling in the final step, a stress gradient occurs in thick ring. In that case, the maximal stress state is away from the contact area. Fig. 7 shows the macroscopic longitudinal transformation strain evolution during the cycle One element of
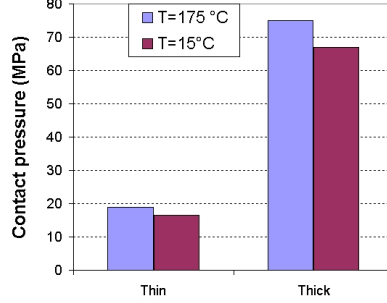
8

Figure 5: Predicted tightening pressure at 175 and 15 °C for thin (left) and thick (right) rings

the thick ring is studied. This strain is obtained by a product between two internal variables, the martensite volume fraction and the mean transformation strain. It can be seen that during the first cooling, the martensite formation does not induce macroscopic transformation strain. The ring opening during internal pressure application is related to the martensite reorientation. The macroscopic longitudinal transformation strain is about 1.28 % and this value the same until the heating. During reverse transformation, the macroscopic longitudinal strain decreases to recover clearance between the two rings, and then induces tightening.

2.4. Experimental investigation

Tightening pressure measurement and cycle

The internal face of the elastic ring is instrumented by three strain gauges positioned in a rosette-like layout. These are thermally self-compensated. The 45 ° strain rosette permits determination of the three independent components of a plane strain tensor, as shown in Fig. 8. An analytical relationship between the tightening pressure and the measured strains is obtained. It allows computations of the tightening pressure induced by $Ni_{47}Ti_{44}Nb_9$ ring on the elastic one. The tightening pressure P generated on the external face of an elastic ring (Young modulus E, internal radius R_i and external radius R_e) depends on internal face axial (ε_z) and tangential (ε_θ) strains, by the Eqn. 9 (Piotrowski, 2010).

$$P = -\frac{E}{2(1+\nu)}\frac{R_e^2 - R_i^2}{R_e^2}(\varepsilon_\theta - \varepsilon_z)$$

(9)

The tests were conducted in Doerler Mesures company. Each test was performed twice for each configuration, the first time with a heating rate of 2 °C/min and a second with a heating rate of 10 °C/min. $Ni_{47}Ti_{44}Nb_9$ and elastic rings are assembled into a climatic chamber as shown in Fig. 9. Heating is applied up to 175 °C, followed by cooling to -30 °C after a stabilization period of 15 minutes. Disassembly is achieved using liquid nitrogen.

Experimental results

Figure 10 shows the contact pressure evolution with temperature in the two configurations. Tn2 and Tck2 are tests conducted respectively with temperature rate of 2 °C/min in thin (Tn) and thick (Tck) configurations, Tn10 and Tck10 are those conducted with 10 °C/min. One can
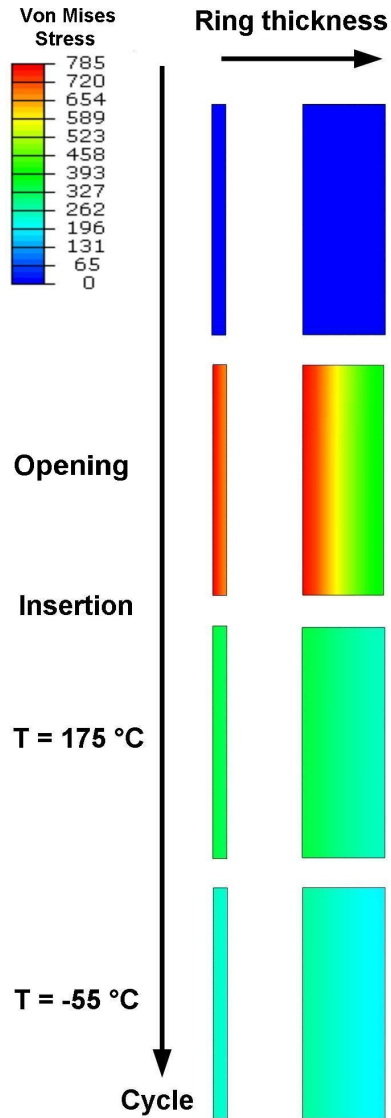
Figure 6: Numerical prediction of stress field into SMA rings at different steps of the studied cycle for thin (left) and thick (right) configurations

see that temperature rate has no influence on results in the thick configuration, whereas there are some differences in the thin one. Three phases are observed:

- Between 30 and 60 °C, a slight increase in tightening pressure of 0.04 MPa/°C is observed.

- Between 65 and 175 °C, an increase of 0.27 MPa/°C is observed in the thin configuration until 120 °C, followed by saturation. In thick configuration, the increase is of 1.6 MPa/°C
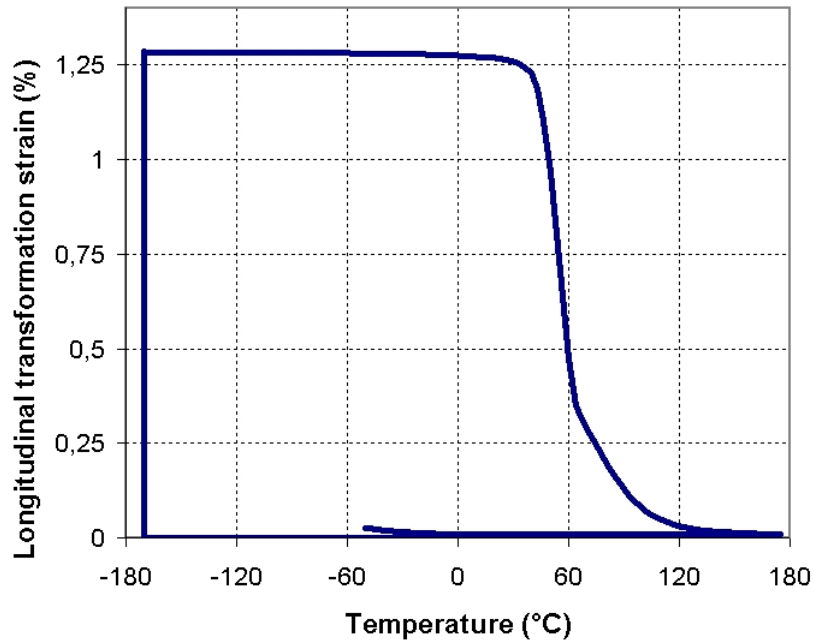
Figure 7: Evolution of the macroscopic longitudinal transformation strain with temperature in a thick ring element
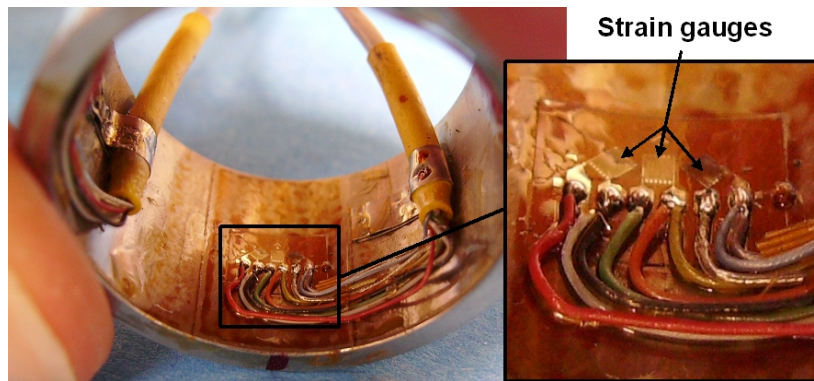
Figure 8: Strain measurement on internal elastic ring with 45 °strain rosette (left) - zoom on the rosette (right)

until 100 °C, followed by a progressive saturation.

- On cooling, between 175 and -28 °C, a very low tightening pressure decrease is observed in the thin configuration (0.015 MPa/°C) while it is a little higher in the thick one (0.12 MPa/°C).
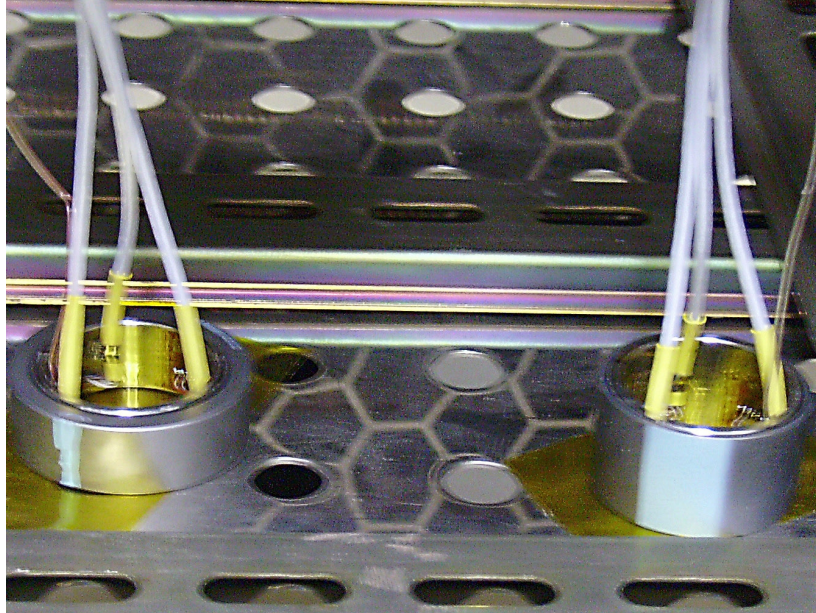
Figure 9: Thin and thick $Ni_{47}Ti_{44}Nb_9$ rings placed around instrumented Inconel 718 elastic rings into climatic chamber in Doerler Mesures company

The first and third phases are due to the difference between the rings thermal expansion: Inconel 718 thermal expansion coefficient is higher than $Ni_{47}Ti_{44}Nb_9$ one. The second phase corresponds to the reverse transformation. The loss of tightening force between the first two phases in the thin configuration corresponds to the reorientation of a part of martensite.

3. Model validation

In this section, numerical predictions are compared with experimental results. This comparison validates the model and highlights its limits. More complex structures are then studied to improve tightening efficiency.

3.1. Experimental/Numerical comparison

Figure 11 shows the comparison between experimental and numerical results for thin (A) and thick (B) devices. In both cases, the temperature at which the contact occurs between SMA and Inconel rings is well predicted, at 60 °C. Once contact is made, the tightening pressure evolution with temperature in experimental study is 0.27 MPa/°C and 1.6 MPa/°C for thin and thick configurations, respectively. The modeled value is about 0.25 MPa/°C in thin case, and 1.6 MPa/°C in thick one which are very close to the experimental ones.

The main difference between experimental and numerical analysis is the saturation, which numerically appears early in both cases and underestimates the generated contact pressure. In the thin configuration, the predicted pressure at the end of heating is 19 MPa while experimental results give 20 MPa. Similarly, predicted and experimental results are 75 and 80 MPa in the thick
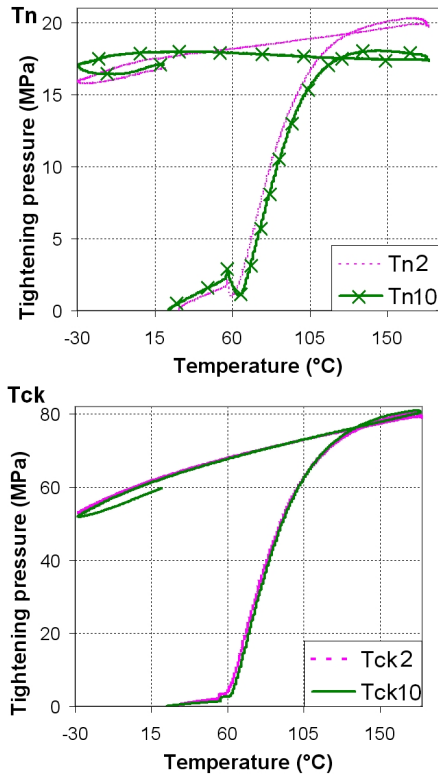
Figure 10: Contact pressure evolution with temperature of thin (Tn) and thick (Tck) $Ni_{47}Ti_{44}Nb_9$ rings on Inconel 718 elastic rings instrumented with strain gages Piotrowski (2010)

configuration. However, the tightening pressure difference never exceeds 7 %.

During cooling, the large temperature hysteresis of $Ni_{47}Ti_{44}Nb_9$ induces the shape memory ring to remain totally austenitic from 175 °C to -30 °C. The behavior of this ring is only governed by thermoelasticity of austenite. Thus, the device can be considered as two thermoelastic rings in contact, with different thermal expansion coefficients. Indeed, $Ni_{47}Ti_{44}Nb_9$ and Inconel 718 thermal expansion coefficients are respectively 8 and 13 $\mu m/(m°C)$. A temperature increase induces a greater expansion of the Inconel 718 inner ring and increases the tightening pressure. Similarly, a temperature decrease induces a decrease of tightening pressure. In the thin ring configuration, the simulated tightening pressure evolution is identical to the experimental one, as 0.015 MPa/°C. However, in the thick one, experimental evolution is 0.12 MPa/°C while the predicted one is about 0.05 MPa/°C. This important difference can be attributed to the analytic equation used to calculate the contact pressure (Eqn. 9) which does not take into account the thermal effect. Another explanation may be the experimental error acquisition performed using a thermocouple placed on the surface of the inner ring, where the temperature is not exactly the same as in the $Ni_{47}Ti_{44}Nb_9$ ring. In both cases, the tightening pressure difference between experimental and numerical analysis is lower than 10 %. Other experiment/model comparisons were performed for various t_R/L_R ratio. Starting from a given ratio, a gradient of plasticity is ob-
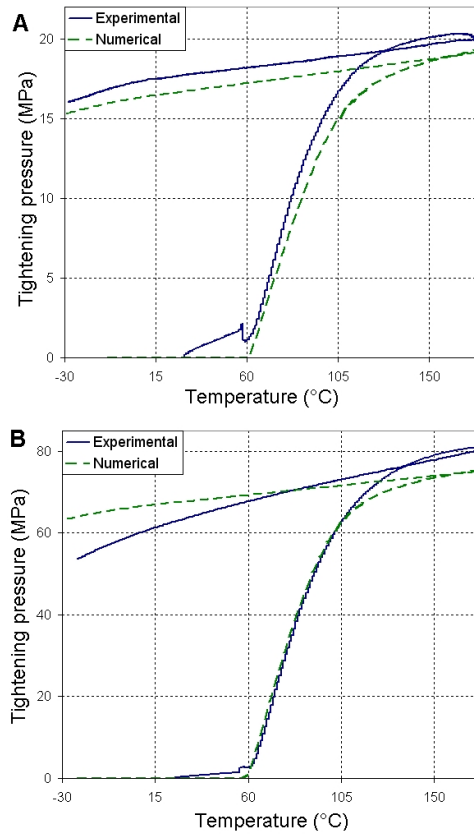
13

Figure 11: Comparison between experimental (heating rate of 2 °C/min) and numerical results for the thin (A) and thick (B) ring devices

served through the thickness during the opening step. This induces a gradient of transformation properties (Liu et al., 2006; Wang et al., 2008) which is not taken into account in the model.

3.2. Complex structure simulations

In order to increase tightening pressure, one solution is to decrease the contact region. The thick ring shape is modified as described in Figure 12. Two ridges are considered. Their emplacement is symmetric following the height direction. The ridge's thickness at the contact region is 1.5 mm. Simulations have been conducted in the same conditions as previous studies. Due to the specific geometry, the discretization around the ridge is important and the tiniest elements length is about 0.5 mm. Figure 13 shows the stress field repartition at the end of the cycle. The ridge structural effect induces an important increase of stress in the elastic ring near the contact area. This stress increase improves tightening efficiency. Nevertheless, two limitations have to be considered. A higher stress level in the SMA induces a higher martensitic transformation temperature. That means that in the final step of the cycle, when the temperature is decreased, the loss of tightening pressure appears early, at higher temperature. This phenomenon is highlighted
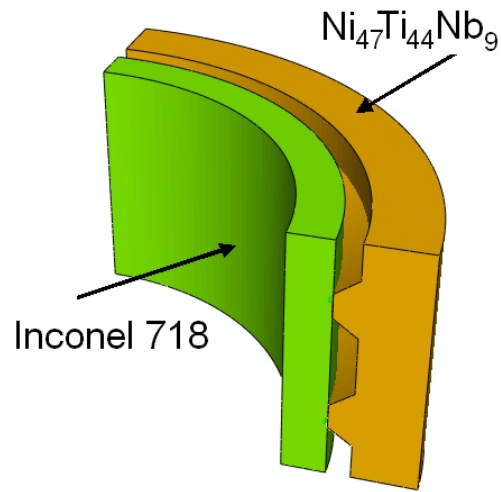
14

Figure 12: 3D representation of modified ring shape to increase tightening pressure. The $Ni_{47}Ti_{44}Nb_9$ ring with ridges (orange) is placed around Inconel 718 ring (green)

by Figure 14 which shows the martensite fraction repartition at the end of heating (a) and at the end of cooling (b). It can be seen that the reverse transformation is fully completed at the end of heating. However, at the end of cooling (-30 °C), martensitic transformation occurs whereas characteristic transformation temperature is lower. The second limitation is the plastic strain of
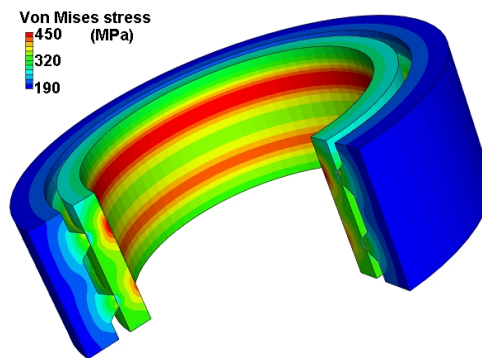
Figure 13: Stress field in a $Ni_{47}Ti_{44}Nb_9$ ring with ridges at the end of the cycle

Inconel 718 ring at the contact region. Indeed, $Ni_{47}Ti_{44}Nb_9$ and Inconel 718 rings have different expansion coefficients. After tightening, a temperature variation induces a different displacement at the contact region. In the elastic domain, Inconel 718 strain can recover this difference. When the total strain is composed of plastic strain, a loss of tightening can be induced. It can be more problematic in sealing applications. These limitations can be easily predicted by finite element simulations. In the present study, ridge thickness and emplacement into the ring are investigated. The Figure 15 highlights the two parameters: 'e', the ridge thickness and 'a', the distance
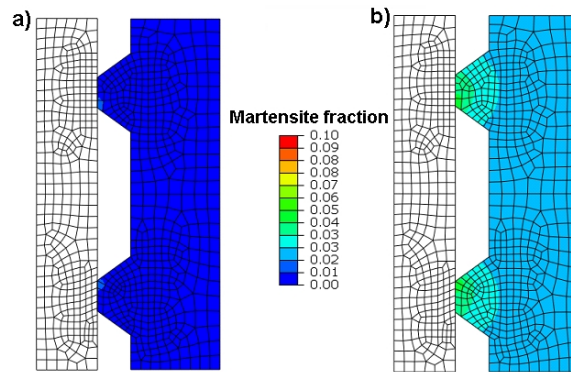
Figure 14: Martensite fraction prediction in the $Ni_{47}Ti_{44}Nb_9$ ring at the end of the cycle - a) at the end of heating (175 °C) - b) at the end of cooling (-30 °C)
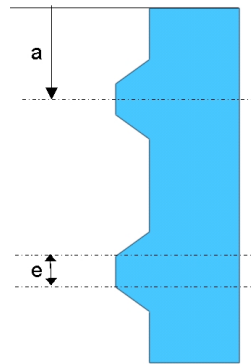

Figure 15: Two studied parameters: 'e', the ridge thickness and 'a', the distance between ridge and ring extremity

between ridge and ring extremity.

Influence of ridge thickness

Five ridge's thicknesses are studied: 0.5, 1, 1.5, 2 and 6 mm. In the last case, thickness is important enough to consider only one ridge, as illustrated in Figure 16. Figure 17 represents the tightening pressure evolution along the contact surface for each case. It can be seen that the thinnest is the ridge thickness, the greatest is the tightening pressure. The maximum contact pressure is 430 MPa when the ridge thickness is about 0.5 mm. An edge effect is highlighted. In the case where there is only one ridge, this phenomenon is clearly identifiable. In areas where there is no edge effect, obtained contact pressure is the same as that found in previous section (without ridge). When the ridge thickness is 1.5, 2 and 6 mm, the maximum tightening pressure is the same, around 280 MPa.
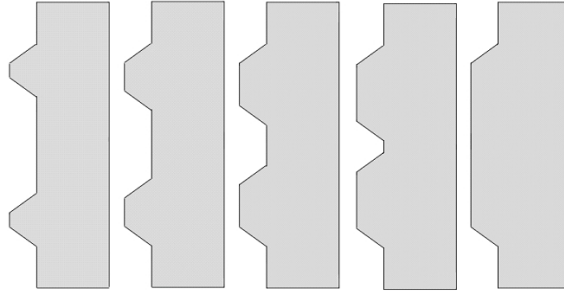
Figure 16: Geometric parameter study: influence of ridge thickness - From left to right: e = 0.5; 1; 1.5; 2; 6
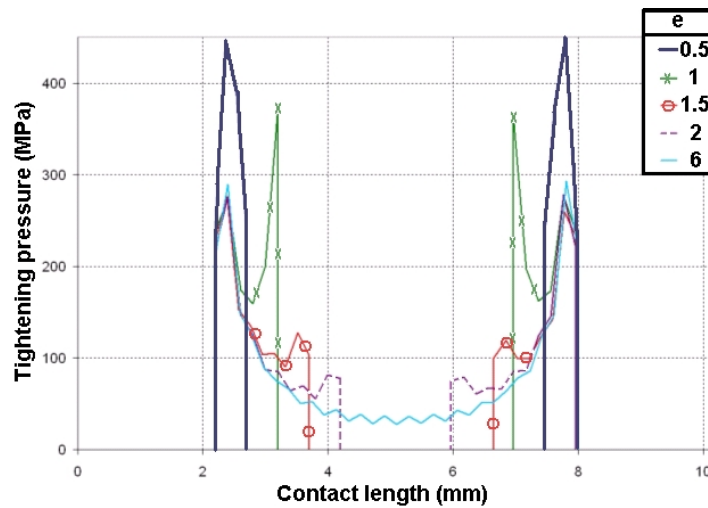

Figure 17: Influence of ridge thickness on tightening pressure - Numerical results for 5 thicknesses: 0.5, 1, 1.5, 2, 6 mm

Influence of distance between ridge and ring extremity

Figure 18 represents cases where distance between ring extremity and ridge is studied. The following values are considered: 0.5, 1 and 2 mm. The 'a' parameter does not exactly influence the maximum tightening pressure, but the pressure spread on the ridge. It can be seen in Figure 19 that the ridge position has an important impact on the maximum tightening pressure, due to a structural effect. When the ridge is near the ring extremity, the maximum tightening pressure is located inside the ridge. Otherwise, when ridges are placed near the ring center, the maximum pressure takes place outside the ridge. An enhanced case has been established where tightening pressure is well distributed on the ridge (a= 1 mm). This parameter is important to control in order to avoid too much stress and unwanted plastic strain.

3.3. Geometrical defect consideration

In previous simulations, a perfect roundness from the shape memory ring has been considered. Nevertheless, an out-of-roundness has been highlighted on supplied rings. It could be
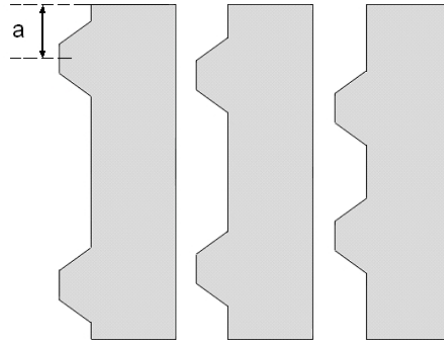
Figure 18: Geometric parameter study: distance between ridge and ring extremity - From left to right: a = 0.5; 1; 2
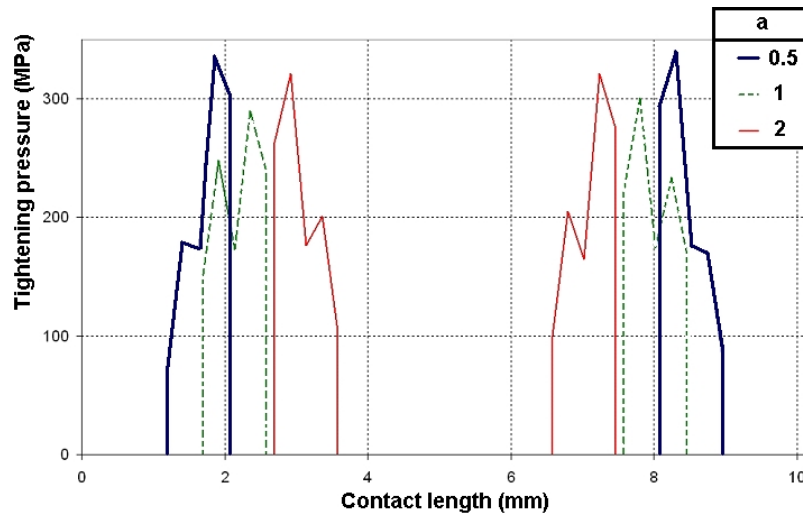

Figure 19: Influence of distance between ring extremity and ridge on tightening pressure - Numerical results for 3 length: 0.5, 1, 2 mm

explained by the protocol used to open the rings. This defect induces a loss of tightening pressure and can induce a loss of sealing in specific applications. With the developed model, this out-of roundness has been taken into account. Figure 20 shows the defect introduced on the thick ring. A difference of 0.1 mm between minimum and maximum internal diameter of the $Ni_{47}Ti_{44}Nb_9$ ring is taken into account, corresponding to a defect/diameter ratio of 0.4 %. The Inconel 718 ring has been modeled with a perfect roundness. In this case, the problem is not axisymmetric, and the developed model has been used in a 3D simulation. Figure 21 represents the stress repartition at the end of the cycle on ring internal face, and Figure 22 compares maximum and minimum tightening pressure with mean pressure. It can be seen that a difference of 0.1 mm on a diameter of 25.4 mm induces an important heterogeneity in tightening pressure. It varies from 100 to 59 MPa at 175 °C. By comparison with mean value around 80 MPa, the difference
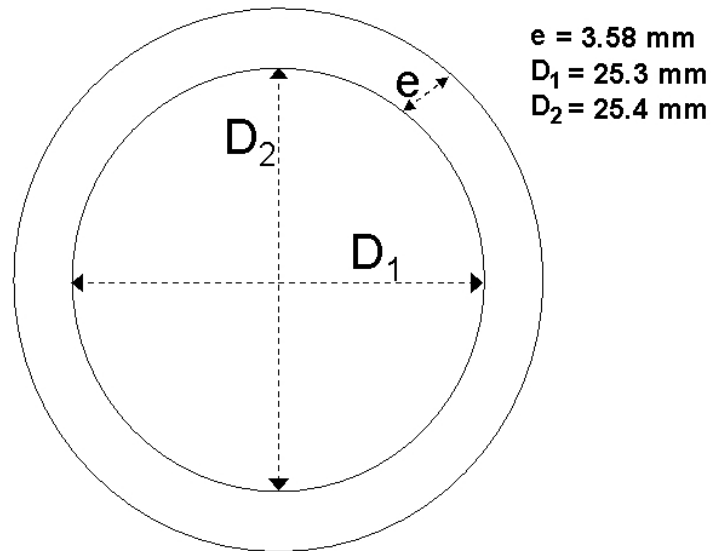
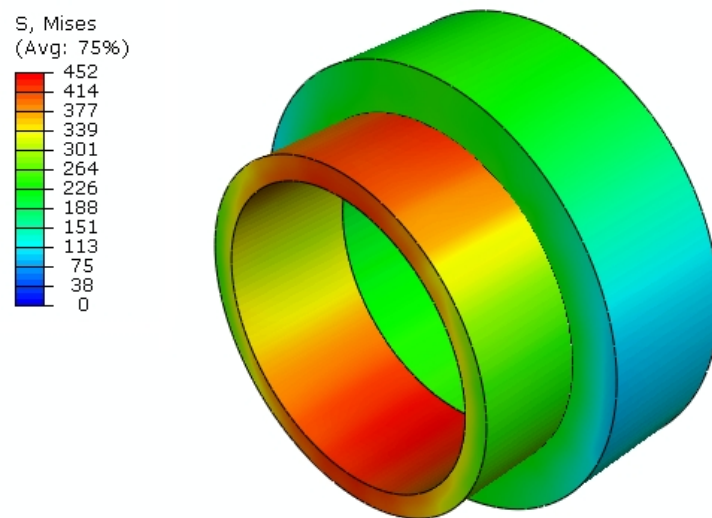Figure 20: Out-of-roundness defect of 0.1 introduced into device finite element model in thick ring case

Figure 21: Heterogeneous stress repartition into SMA ring due to out-of-roundness

is about 25 %. It can be noticed that mean tightening pressure of 80 MPa is the value obtained in axisymmetric model without out-of-roundness.
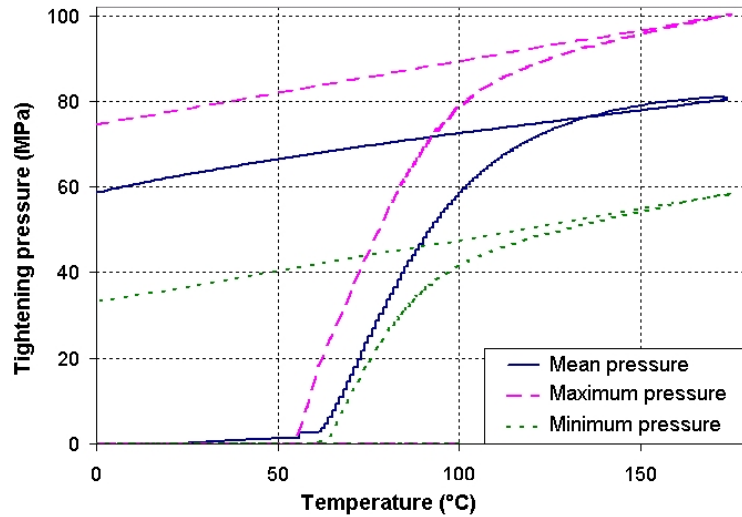
19

Figure 22: Maximum and minimum tightening pressure evolution - Comparison with mean pressure

4. Conclusion

A thermomechanical model developed elsewhere and implemented into the finite element software ABAQUS® is used to describe the response of tightening rings made in $Ni_{47}Ti_{44}Nb_9$ shape memory alloys. The validation strategy of this model has been presented and an experimental database has been produced using a test bed developed in this work. Comparisons with these experimental results show an accurate prediction of the rings tightening pressure.

This validation allows using this numerical tool for industrial applications design to optimize the component shape or to consider the influence of geometric defects like out-of-roundness. A parametric analysis was performed to determine ridge effect on tightening pressure. The following trends have been identified:

- Presence of ridges in SMA rings improves the tightening.

- Thinnest ridges induce a higher tightening pressure.

- In SMA rings with two ridges, an enhanced positioning of these ridges is determined.

- An out-of-roundness defect of 0.4 % is enough to induce a local decrease as large as 25 % in the tightening pressure

These trends are very important for SMA component design. These results are very promising and further investigations are needed to extend the domain of validity of the model considered in this study.

Model validation has been performed in the temperature range of -30 to 175 °C. However, it could be interesting to extend this domain to temperatures below -30 °C to be able to consider specific transport requirements. One of the main limitations of the model is that it does not take into account the occurrence of plasticity in the SMA. This excludes accurate prediction for high

stress domain when stress exceeds the NiTi matrix plastic yield stress. This case is encountered during the opening step of very thick rings. Further investigations are conducted in order to take into account the effect of a plasticity gradient in NiTi matrix, and material parameter evolution with plastic strain.   *Acknowledgement* - This research has been performed within a project

References

Chemisky, Y., Duval, A., Patoor, E., Ben Zineb, T., 2011. Shape Memory Alloys modeling, including phase transformation and twinning effects. Mechanics of Materials (under review).

Chemisky, Y., Duval, A., Piotrowski, B., Ben Zineb, T., Tahiri, V., Patoor, E., 2009. Numerical tool for SMA materials simulation - Application to composite structures design. Smart Materials and Structures 1, 1–2.

De la Flor, S., Urbina, C., Ferrando, F., 2006. Constitutive model of shape memory alloys: Theoretical formulation and experimental validation. Materials Science and Engineering A 427, 112–122.

Hartl, D. J., Chatzigeorgiou, G., Lagoudas, D., 2010. Three-dimensional modeling and numerical analysis of rate-dependent irrecoverable deformation in shape memory alloys. International Journal of Plasticity 26, 1485–1507.

He, X. M., Zhao, L. Z., Zhang, S. F., Duo, S. W., Zhang, R. F., 2006. Study of the thermal physical properties of $Ti_{44}Ni_{47}Nb_9$ wide hysteresis shape memory alloys. Materials Science and Engineering A 441, 167–169.

Kauffman, G. B., Mayo, I., 1996. The Story of Nitinol: The Serendipitous Discovery of the Memory Metal and Its Applications. The Chemical Educator 2, 1–21.

Liu, Y., Mahmud, A., Kursawe, F., Nam, T. H., 2006. Effect of pseudoelastic cycling on the Clausius-Clapeyron relation for stress-induced martensitic transformation in NiTi. Journal of Alloys and Compounds 449, 82–87.

Melton, K. N., Proft, J. L., Duerig, T. W., 1989. Wide Hysteresis Shape Memory Alloys Based on the NiTiNb System. The Martensitic Transformation in Science and Technology., 191–198.

Miyazaki, S., Ohmi, Y., Otsuka, K., Suzuki, Y., 1982. Characteristics of deformation and transformation pseudoelasticity in Ti-Ni alloys. Journal de Physique 44, C4–255.

Nemat-Nasser, S., Guo, W. G., 2000. Flow stress of commercially pure niobium over a broad range of temperatures and strain rates. Materials Science and Engineering A 284, 202–210.

Panico, M., Brinson, L. C., 2007. A three-dimensional phenomenological model for martensite reorientation in shape memory alloys. Journal of the Mechanics and Physics of Solids 55, 2491–2511.

Peultier, B., Ben Zineb, T., Patoor, E., 2006. Macroscopic constitutive law of shape memory alloy thermomechanical behaviour. Application to structure computation by FEM. Mechanics of Materials 38, 510–524.

Peultier, B., Ben Zineb, T., Patoor, E., 2008. Macroscopic constitutive law for SMA: Application to structure analysis by FEM. Materials Science and Engineering A 438-440, 454–458.

Piotrowski, B., 2010. Analyse numérique et expérimentale du comportement d'un alliage à mémoire de forme avec précipités ($Ni_{47}Ti_{44}Nb_9$) : application à la connectique. Phd thesis, Nancy University.

Piotrowski, B., Ben Zineb, T., Patoor, E., Eberhardt, A., 2011. Modeling of niobium precipitates effect on the $ni_{47}ti_{44}nb_9$ shape memory alloy behavior. Submitted to International Journal of Plasticity.

Saint-Sulpice, L., Arbab Chirani, S., Calloch, S., 2009. A 3D super-elastic model for shape memory alloys taking into account progressive strain under cyclic loadings. Mechanics of Materials 41, 12–26.

Simo, J. C., Hughes, T. J. R., 2000. Computational Inelasticity. Springer.

Videnic, T., Kosel, F., Puksic, A., Brojan, M., 2007. A Phenomenological Two-Dimensional Model of Constrained Recovery in Shape Memory Alloy Rings. Proceedings of the 2nd IASME / WSEAS International Conference on Continuum Mechanics (CM'07), Portoroz, Slovenia.

Vieille, B., Michel, J. F., Boubakar, M. L., Lexcellent, C., 2007. Validation of a 3D numerical model of shape memory alloys pseudoelasticity through tensile and bulging tests on CuAlBe sheets. International Journal of Mechanical Sciences 49, 280–297.

Wang, X., Xu, B., Yeu, Z., 2008. Phase transformation behavior of pseudoelastic NiTi shape memory alloys under large strain. Journal of Alloys and Compounds 463, 417–422.

Wilkins, M. L., 1964. Calculation of Elastic-Plastic Flow. Methods of Computational Physics.

Xiao, F., Ma, G., Zhao, X., Xu, H., Jiang, H., Rong, L., 2008. A novel TiNiNb shape memory alloy with high yield strength and high damping capacity. International Conference on Smart Materials and Nanotechnology in Engineering.

Zaki, W., Moumni, Z., 2007. A three-dimensional model of the thermomechanical behavior of shape memory alloys. Journal of the Mechanics and Physics of Solids 55, 2455–2490.

Zhang, C. S., Wang, Y. Q., Chai, W., Zhao, L. C., 1991. The study of constitutional phases in a $Ni_{47}Ti_{44}Nb_9$ shape memory alloy. Materials Chemistry and Physics 28, 43–50.